

Capacity Analysis on OAM-Based Wireless Communications: An Electromagnetic Information Theory Perspective

Runyu Lyu, *Student Member, IEEE*, Wenchi Cheng, *Senior Member, IEEE*, Qinghe Du, *Member, IEEE*, and Tony Quek, *Fellow, IEEE*

Abstract—Orbital angular momentum (OAM) technology enhances the spectrum and energy efficiency of wireless communications by enabling multiplexing over different OAM modes. However, classical information theory, which relies on scalar models and far-field approximations, cannot fully capture the unique characteristics of OAM-based systems, such as their complex electromagnetic field distributions and near-field behaviors. To address these limitations, this paper analyzes OAM-based wireless communications from an electromagnetic information theory (EIT) perspective, integrating electromagnetic theory with classical information theory. EIT accounts for the physical properties of electromagnetic waves, offering advantages such as improved signal manipulation and better performance in real-world conditions. Given these benefits, EIT is more suitable for analyzing OAM-based wireless communication systems. Presenting a typical OAM model utilizing uniform circular arrays (UCAs), this paper derives the channel capacity based on the induced electric fields by using Green’s function. Numerical and simulation results validate the channel capacity enhancement via exploration under EIT framework. Additionally, this paper evaluates the impact of various parameters on the channel capacity. These findings provide new insights for understanding and optimizing OAM-based wireless communications systems.

Index Terms—Orbital angular momentum (OAM), electromagnetic information theory (EIT).

I. INTRODUCTION

ORBITAL angular momentum (OAM) [1] refers to the angular momentum carried by electromagnetic waves around their propagation axis. In both optical and radio-frequency communications, OAM enhances spectrum efficiency by enabling multiplexing and demultiplexing over different OAM modes [2]–[5] and can improve energy efficiency as well [6]. However, classical information theory (CIT) [7] has limitations when applied to OAM-based wireless communication systems due to the unique characteristics of OAM beams and the complexities involved in practical implementation. For example, CIT cannot fully account for the

physical properties of electromagnetic waves, as it typically relies on scalar quantities, far-field approximations, discrete models, and other non-physically consistent assumptions [8]. These assumptions are unsuitable for OAM-based wireless communication, which relies on the special structure of electromagnetic field distributions of OAM beams, emphasizes near-field characteristics, and is inherently more continuous than traditional multiple-input multiple-output (MIMO) systems [9], [10]. Additionally, while CIT provides a framework for calculating channel capacity, it can not fully capture the potential capacity gains achievable with OAM multiplexing due to the unique spatial properties of OAM beams. Studies on OAM capacity, such as [11], use free-space channel matrices to analyze the channel capacity of OAM-based systems, reveal that communicating over the sub-channels of OAM modes can be considered a subset of MIMO and offer no additional capacity gains compared to MIMO. However, these studies do not account for the distinctive beam characteristics of OAM beams, leaving open the question of whether potential benefits have been overlooked. Therefore, a new approach that integrates electromagnetic theory and CIT is needed to study OAM-based wireless communications.

Electromagnetic information theory (EIT) [12], [13] is a new branch of information theory. It studies the transmission and processing of information through electromagnetic waves, integrating electromagnetic theory and CIT, which makes it capable of addressing the limitations of CIT and solving new challenges in an era where data demands are increasing [14]–[16]. EIT offers several advantages over CIT. First, EIT, emphasizing physical layer phenomena, provides new opportunities for signal manipulation and transmission strategies that are not typically addressed in CIT [17]. Secondly, EIT allows for a more comprehensive analysis of channel capacity by considering the physical characteristics of electromagnetic waves, which can lead to improved data and robustness performance in real-world scenarios [8]. Additionally, EIT supports the integration of advanced technologies, such as continuous-aperture MIMO (CAP-MIMO) [18], [19] and reconfigurable intelligent surfaces (RISs) [20], [21]. These technologies exploit the spatial and temporal degrees of freedom offered by electromagnetic waves, which are often overlooked in classical approaches. Due to its advantages over CIT, EIT is more suitable for analyzing OAM-based wireless communication systems.

In this paper, we analyze OAM-based wireless communi-

Runyu Lyu and Wenchi Cheng are with School of Telecommunications Engineering, Xidian University, Xi’an, 710071, China (e-mails: rylv@stu.xidian.edu.cn; wccheng@xidian.edu.cn).

Qinghe Du is with School of Information and Communications Engineering, Xi’an Jiaotong University, Xi’an, 710049, China (e-mail: duqinghe@mail.xjtu.edu.cn).

Tony Q.S. Quek is with Information Systems Technology and Design, Singapore University of Technology and Design, Singapore, 487372, Singapore (e-mail: tonyquek@sutd.edu.sg).

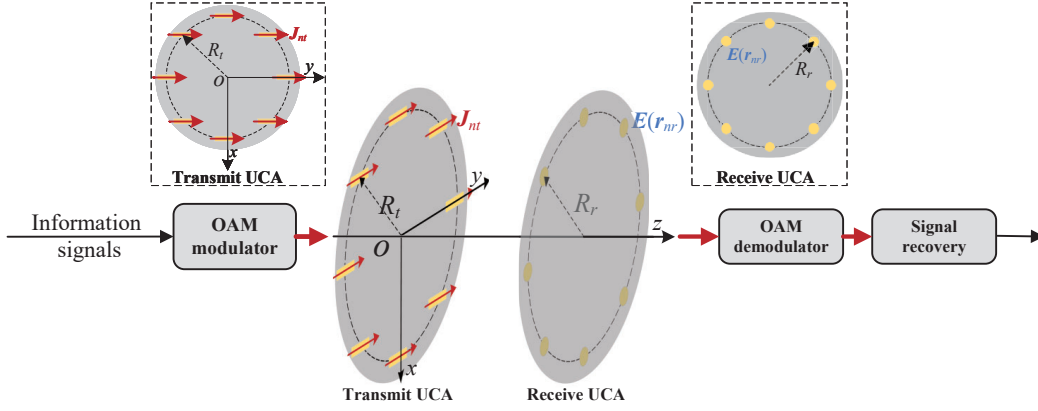


Fig. 1. EIT based OAM wireless communication system model.

communications from an EIT perspective. We first propose a system model of OAM-based wireless communications based on uniform circular array (UCA) to provide an intuitive and concise analysis environment. Then, we give the induced electric field by using Green's function for continuous regions and derive the expression for the induced electric field of received OAM signal. Based on the induced electric field, we derive the channel capacity for the OAM-based wireless communication by presenting the autocorrelation and cross-correlation functions of the received OAM signals. Numerical and simulation results validate the channel capacity enhancement via exploration under EIT framework. We also analyze the impacts of different parameters on capacity, including numbers of transmitting and receiving mode, transmit and receive UCA distance, and UCA radii.

The rest of the paper is organized as follows. Section II gives the OAM-based wireless communication system model. Section III derives the induced electric field of OAM signals. Channel capacity of the OAM-based wireless communication is derived in Section IV. Sections V and VI give numerical and simulation results. The conclusion is given in Section VII.

Notation : Matrices and vectors are denoted by letters in bold. The notations “ $(\cdot)^*$ ” and “ $(\cdot)^H$ ” denote the conjugation and Hermitian, of a matrix or vector, respectively.

II. SYSTEM MODEL

Figure 1 shows the OAM wireless communication system model analyzed from an EIT perspective, where N_t OAM modes are used for multiplexing and N_r OAM modes for demultiplexing. A UCA, consisting of N_t linear sources, is employed as the transmit source. The length of each linear source is set to half the wavelength and aligned along the y -axis. The current density at the n_t th transmit source is denoted by $\mathbf{J}_{n_t} \in \mathbb{C}^{3 \times 1}$, which is also aligned along the y -axis. The receiver is also a UCA, but consisting of N_r point antennas. The induced electric field at the n_r th receive point is represented as $\mathbf{E}_{r_{n_r}} \in \mathbb{C}^{3 \times 1}$, where $\mathbf{r}_{n_r} \in \mathbb{R}^{3 \times 1}$ denotes the coordinates of the n_r th receive point. The radii of the transmit and receive UCAs are denoted by R_t and R_r , respectively. UCAs are selected due to their ability to digitally generate OAM beams with a uniform radius and common center [22]. However, it should be noted that other antenna types, such as spiral phase plates or metasurfaces

with different geometries, can also be used to generate OAM beams. As depicted in Fig. 1, the multi-stream RF information signals are first modulated, allocated power across different OAM modes, and then transmitted via the transmit UCA. The induced electric field is generated at the receive UCA, where the signals are demodulated to extract the OAM-modulated information.

III. ANALYSIS ON OAM WIRELESS COMMUNICATIONS FROM EIT PERSPECTIVE

In this section, we first present the induced electric field by using Green's function for continuous regions. Following this, we derive the expression for the induced electric field of OAM-based system as well as the received OAM signal. Finally, we provide some figures of the induced electric field for different OAM modes.

A. Wireless Communication of Continuous Regions

In EIT, Green's function can be used to model the wireless communication between two continuous regions. Let $\mathbf{J}(\mathbf{s}) \in \mathbb{C}^{3 \times 1}$ and $\mathbf{E}(\mathbf{r}) \in \mathbb{C}^{3 \times 1}$ denote the current density at the source and the induced electric field at the destination respectively, where $\mathbf{s} \in \mathbb{R}^{3 \times 1}$ represents the coordinate of the source and $\mathbf{r} \in \mathbb{R}^{3 \times 1}$ represents the coordinate of the field observer. The induced electric field can be derived through the current density by using Green's function as follows:

$$\mathbf{E}(\mathbf{r}) = \int_{V_s} \mathbf{G}(\mathbf{r}, \mathbf{s}) \mathbf{J}(\mathbf{s}) d\mathbf{s}, \quad \mathbf{r} \in V_r, \quad (1)$$

where $\mathbf{G}(\mathbf{r}, \mathbf{s}) \in \mathbb{C}^{3 \times 3}$ denotes the Green's function, V_s denotes the source space, and V_r denotes the received space. In unbounded, homogeneous mediums at a fixed frequency point, the Green's function can be simplified as follows [23]:

$$\begin{aligned} \mathbf{G}(\mathbf{r}, \mathbf{s}) &= \frac{jk_0 Z_0}{4\pi \|\mathbf{p}\|} \left(\mathbf{I}_3 + \frac{\nabla_{\mathbf{r}} \nabla_{\mathbf{r}}^H}{k_0^2} \right) e^{jk_0 \|\mathbf{p}\|} \\ &\approx \frac{jk_0 Z_0 e^{jk_0 \|\mathbf{p}\|}}{4\pi \|\mathbf{p}\|} \left[(\mathbf{I}_3 - \hat{\mathbf{p}} \hat{\mathbf{p}}^H) \right. \\ &\quad \left. + \frac{j\lambda}{2\pi \|\mathbf{p}\|} (\mathbf{I}_3 - 3\hat{\mathbf{p}} \hat{\mathbf{p}}^H) \right. \\ &\quad \left. - \left(\frac{\lambda}{2\pi \|\mathbf{p}\|} \right)^2 (\mathbf{I}_3 - 3\hat{\mathbf{p}} \hat{\mathbf{p}}^H) \right], \quad (2) \end{aligned}$$

where j denotes the imaginary unit, k_0 represents the wave number, Z_0 denotes the free-space intrinsic impedance, $\mathbf{p} = \mathbf{r} - \mathbf{s}$ denotes the distance vector, $\|\mathbf{p}\|$ does the l^2 -norm of \mathbf{p} , $\hat{\mathbf{p}} = \mathbf{p}/\|\mathbf{p}\|$ denotes the distance unit vector, \mathbf{I}_3 denotes an identity matrix of size 3×3 , and λ represents the wave length.

B. Analysis on OAM Wireless Communications Based on EIT

Considering the OAM wireless communications as shown in Fig. 1, the current densities of the sources are along the y -axis and are given by multiplying the multi-stream RF information signal, denoted by $\mathbf{x} \in \mathbb{C}^{N_t \times 1}$, with a normalized IDFT matrix, denoted by $\mathbf{W} \in \mathbb{C}^{N_t \times N_t}$ with the n_1 th row and the n_2 th column element given by $W_{n_1, n_2} = \frac{1}{\sqrt{N_t}} \exp[j2\pi(n_1-1)(n_2-1)/N_t]$. Thus, the obtained current density of the n_t th transmit source can be given as follows:

$$\mathbf{J}_{n_t} = \mathbf{J}_{n_t} \cdot \hat{\mathbf{e}}_y = J_{n_t}^y = \frac{1}{\sqrt{N_t}} \sum_{m=1}^{N_t} x(m) e^{j2\pi(m-1)(n_t-1)/N_t}, \quad (3)$$

where $\hat{\mathbf{e}}_y = [0, 1, 0]^T$ denotes the unit vector along y coordinate, $J_{n_t}^y$ represents the y component for the current density of the n_t th transmit source, and $x(m)$ denotes the m th element of \mathbf{x} . Thus, Eq. (1) can be rewritten as follows:

$$\begin{aligned} \mathbf{E}(\mathbf{r}) &= \int_{V_{s, n_t}} \mathbf{G}(\mathbf{r}, \mathbf{s}) \mathbf{J}(\mathbf{s}) d\mathbf{s} \\ &= \sum_{n_t=1}^{N_t} \int_{R_t \sin(\frac{2\pi n_t}{N_t}) - \frac{L}{2}}^{R_t \sin(\frac{2\pi n_t}{N_t}) + \frac{L}{2}} \mathbf{G}(\mathbf{r}, \mathbf{s}) J_{n_t}^y ds^y \\ &= \sum_{n_t=1}^{N_t} J_{n_t}^y \int_{y_{n_t} - \frac{L}{2}}^{y_{n_t} + \frac{L}{2}} \begin{bmatrix} G^{xy}(\mathbf{r}, \mathbf{s}) \\ G^{yy}(\mathbf{r}, \mathbf{s}) \\ G^{zy}(\mathbf{r}, \mathbf{s}) \end{bmatrix} ds^y, \quad \mathbf{s} \in V_{s, n_t}, \end{aligned} \quad (4)$$

where V_{s, n_t} denotes the source space of the n_t th antenna, s^y denotes the y coordinate of \mathbf{s} , $y_{n_t} = R_t \sin(\frac{2\pi n_t}{N_t})$ denotes the y coordinate of the n_t th transmit source, $G^{xy}(\mathbf{r}, \mathbf{s})$, $G^{yy}(\mathbf{r}, \mathbf{s})$, and $G^{zy}(\mathbf{r}, \mathbf{s})$ denote the first, second, and third elements in the second column of $\mathbf{G}(\mathbf{r}, \mathbf{s})$ respectively. When using high-resolution discrete lens arrays to form a quasi-continuous aperture phased UCA, Eq. (4) can be rewritten into a discrete form as follows:

$$\mathbf{E}(\mathbf{r}) = \frac{1}{N_l} \sum_{n_t=1}^{N_t} \sum_{n_l=1}^{N_l} \begin{bmatrix} G^{xy}(\mathbf{r}, \mathbf{s}_{n_t, n_l}) \\ G^{yy}(\mathbf{r}, \mathbf{s}_{n_t, n_l}) \\ G^{zy}(\mathbf{r}, \mathbf{s}_{n_t, n_l}) \end{bmatrix} J_{n_t}^y, \quad (5)$$

where \mathbf{s}_{n_t, n_l} denotes the coordinate for the n_l th small feed of the n_t th transmit source in the UCA and s_{n_t, n_l}^y is the y coordinate of \mathbf{s}_{n_t, n_l} . The value of s_{n_t, n_l} is given as follows:

$$\mathbf{s}_{n_t, n_l} = \begin{bmatrix} R_t \cos(\frac{2\pi n_t}{N_t}) \\ R_t \sin(\frac{2\pi n_t}{N_t}) + \frac{n_l-1}{N_l-1} L - \frac{L}{2} \\ 0 \end{bmatrix}. \quad (6)$$

As shown in Fig. 1, the received signal is given as the received induced electric field multiplied with a normalized DFT matrix. Therefore, the l th received OAM signal, denoted

by y_l , is given by performing DFT on the induced electric field at receive points as follows:

$$\mathbf{y}_l = \frac{1}{\sqrt{N_r}} \sum_{n_r=1}^{N_r} \mathbf{E}(\mathbf{r}_{n_r}) e^{j2\pi l(n_r-1)/N_r} + \mathbf{n}, \quad (7)$$

where \mathbf{n} denotes the additive noise.

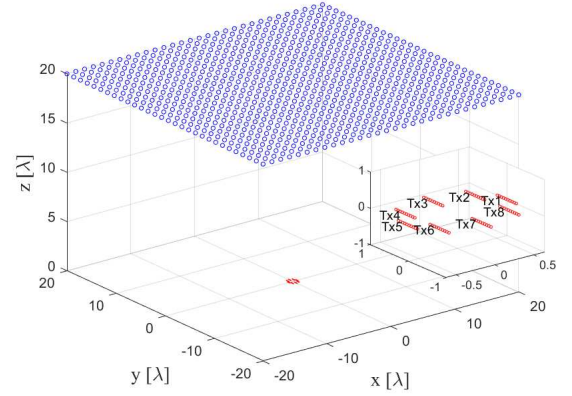


Fig. 2. Transmit UCA and observer schematic.

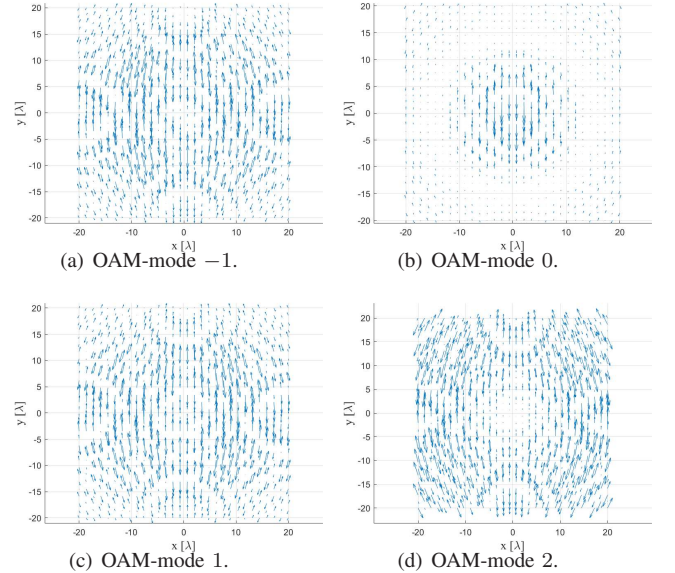


Fig. 3. Electric fields of OAM-mode -1 , 0 , 1 , and 2 .

To better illustrate the induced electric field of the OAM signals, we deploy a grid of 100×100 virtual receive points on a plane located 20λ (1034.5 mm) away from the transmit UCA as shown in Fig. 2. The frequency is set to 5.8 GHz. The width of the observer plane is also set to 20λ . The number of transmit sources is set to 8 , each consisting of 30 small feeds. The current density is normalized by dividing it by $\sqrt{240}$ for each feed. The length of each transmit source is set to 0.5λ (25.9 mm) and the radius of the transmit UCA is set to $2\lambda/\pi$ (32.9 mm). Based on the above settings, Fig. 3 presents the induced electric fields for OAM modes -1 to 2 with the phase set to 0 deg. As shown in the figure, the induced electric

fields are primarily oriented along the y -axis, same to the current densities at the source. Fig. 3 also highlights the hollow divergence phenomenon characteristic of OAM transmissions.

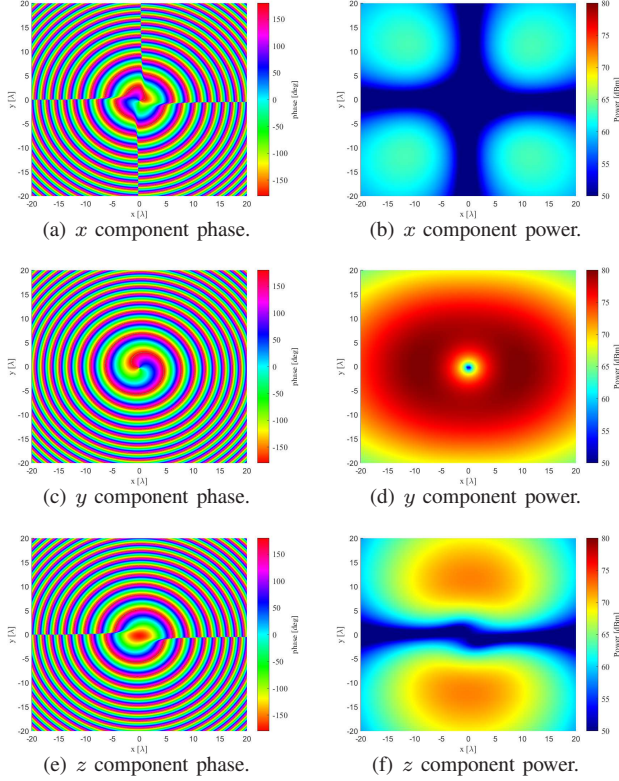


Fig. 4. x , y , and z components of power and phase for OAM-mode 1.

We also plot the x , y , and z components of the power and phase for OAM mode 1 in Fig. 4 based on the same setting in Fig. 2. As shown in this figure, the power of the y -component is significantly higher than that of the x and z -components, indicating that the primary direction of the induced electric field aligns with the current density direction of the source. The typical spiral phase structure of OAM beams is also observed in the y -direction. Additionally, Fig. 4 highlights the hollow divergence of OAM beams.

IV. CHANNEL CAPACITY DERIVATION UNDER EIT FRAMEWORK

In this section, we derive the channel capacity for the OAM-based wireless communications from an EIT perspective. We begin by presenting the autocorrelation and cross-correlation functions of the received OAM signals. Based on the cross-correlation matrix of the received OAM signals, we then calculate the channel capacity.

A. Autocorrelation and Cross-correlation Functions of Received OAM Signals

The cross-correlation function between the n_t th and n'_t th y component current density, denoted by $\mathbf{R}_{J_{n_t}^y, J_{n'_t}^y} =$

$\mathbb{E} \left\{ J_{n_t}^y (J_{n'_t}^y)^* \right\}$, can be give as follows:

$$\begin{aligned} \mathbf{R}_{J_{n_t}^y, J_{n'_t}^y} &= \mathbb{E} \left\{ \frac{1}{\sqrt{N_t}} \sum_{m=1}^{N_t} x(m) e^{\frac{j2\pi(m-1)(n_t-1)}{N_t}} \right. \\ &\quad \left. \frac{1}{\sqrt{N_t}} \sum_{m'=1}^{N_t} x^*(m') e^{-\frac{j2\pi(m'-1)(n'_t-1)}{N_t}} \right\} \\ &= \frac{1}{N_t} \sum_{m=1}^{N_t} \sum_{m'=1}^{N_t} \mathbb{E} \{ x(m) x^*(m') \} \\ &\quad e^{\frac{j2\pi(mn_t - m'n'_t - m + m' - n_t + n'_t)}{N_t}}. \end{aligned} \quad (8)$$

For normalized input signals independent from each other, we have $\mathbb{E} \{ \mathbf{x} \mathbf{x}^H \} = \mathbf{I}_{N_t}$. Therefore, Eq. (8) can be rewritten as follows:

$$\mathbf{R}_{J_{n_t}^y, J_{n'_t}^y} = \frac{1}{N_t} \sum_{m=1}^{N_t} e^{\frac{j2\pi(m-1)(n_t-n'_t)}{N_t}} = \begin{cases} 0, & n_t \neq n'_t \\ 1, & n_t = n'_t. \end{cases} \quad (9)$$

Base on Eq. (4), the autocorrelation function of induced electric field, denoted by $\mathbf{R}_{\mathbf{E}}(\mathbf{r}, \mathbf{r}') = \mathbb{E} \left\{ \mathbf{E}(\mathbf{r}) \mathbf{E}^H(\mathbf{r}') \right\}$, can be derived as follows:

$$\begin{aligned} \mathbf{R}_{\mathbf{E}}(\mathbf{r}, \mathbf{r}') &= \mathbb{E} \left\{ \left[\sum_{n_t=1}^{N_t} J_{n_t}^y \int_{y_{n_t}-\frac{L}{2}}^{y_{n_t}+\frac{L}{2}} \begin{bmatrix} G^{xy}(\mathbf{r}, \mathbf{s}) \\ G^{yy}(\mathbf{r}, \mathbf{s}) \\ G^{zy}(\mathbf{r}, \mathbf{s}) \end{bmatrix} ds^y \right] \right. \\ &\quad \left. \left[\sum_{n'_t=1}^{N_t} J_{n'_t}^y \int_{y_{n'_t}-\frac{L}{2}}^{y_{n'_t}+\frac{L}{2}} \begin{bmatrix} G^{xy}(\mathbf{r}', \mathbf{s}') \\ G^{yy}(\mathbf{r}', \mathbf{s}') \\ G^{zy}(\mathbf{r}', \mathbf{s}') \end{bmatrix} ds'^y \right]^H \right\} \\ &= \sum_{n_t=1}^{N_t} \sum_{n'_t=1}^{N_t} \mathbf{R}_{J_{n_t}^y, J_{n'_t}^y} \int_{y_{n_t}-\frac{L}{2}}^{y_{n_t}+\frac{L}{2}} \int_{y_{n'_t}-\frac{L}{2}}^{y_{n'_t}+\frac{L}{2}} \\ &\quad \begin{bmatrix} G^{xy}(\mathbf{r}, \mathbf{s}) \\ G^{yy}(\mathbf{r}, \mathbf{s}) \\ G^{zy}(\mathbf{r}, \mathbf{s}) \end{bmatrix} \begin{bmatrix} G^{xy}(\mathbf{r}', \mathbf{s}') \\ G^{yy}(\mathbf{r}', \mathbf{s}') \\ G^{zy}(\mathbf{r}', \mathbf{s}') \end{bmatrix}^H ds^y ds'^y, \\ &\quad \mathbf{r}, \mathbf{r}' \in V_r, \mathbf{s} \in V_{s, n_t}, \mathbf{s}' \in V_{s, n'_t}. \end{aligned} \quad (10)$$

Substitute Eq. (9) into Eq. (10), the autocorrelation function of induced electric field can be given as follows:

$$\mathbf{R}_{\mathbf{E}}(\mathbf{r}, \mathbf{r}') = \sum_{n_t=1}^{N_t} \int_{y_{n_t}-\frac{L}{2}}^{y_{n_t}+\frac{L}{2}} \int_{y_{n_t}-\frac{L}{2}}^{y_{n_t}+\frac{L}{2}} \begin{bmatrix} G^{xy}(\mathbf{r}, \mathbf{s}) \\ G^{yy}(\mathbf{r}, \mathbf{s}) \\ G^{zy}(\mathbf{r}, \mathbf{s}) \end{bmatrix} \begin{bmatrix} G^{xy}(\mathbf{r}', \mathbf{s}') \\ G^{yy}(\mathbf{r}', \mathbf{s}') \\ G^{zy}(\mathbf{r}', \mathbf{s}') \end{bmatrix}^H ds^y ds'^y. \quad (11)$$

The discrete form of Eq. (11) can be given as follows:

$$\mathbf{R}_{\mathbf{E}}(\mathbf{r}, \mathbf{r}') = \frac{1}{N_t^2} \sum_{n_t=1}^{N_t} \sum_{n_l=1}^{N_t} \sum_{n'_l=1}^{N_t} \begin{bmatrix} G^{xy}(\mathbf{r}, \mathbf{s}_{n_t, n_l}) \\ G^{yy}(\mathbf{r}, \mathbf{s}_{n_t, n_l}) \\ G^{zy}(\mathbf{r}, \mathbf{s}_{n_t, n_l}) \end{bmatrix} \begin{bmatrix} G^{xy}(\mathbf{r}, \mathbf{s}_{n_t, n'_l}) \\ G^{yy}(\mathbf{r}, \mathbf{s}_{n_t, n'_l}) \\ G^{zy}(\mathbf{r}, \mathbf{s}_{n_t, n'_l}) \end{bmatrix}^H. \quad (12)$$

Based on Eq. (7) and let the noise independent of the signals, the cross-correlation function between the received

signals of the l th and l' th OAM modes, denoted by $\mathbf{R}_y(l, l') = \mathbb{E} \{y_l y_{l'}^H\}$, can be derived as follows:

$$\begin{aligned} \mathbf{R}_y(l, l') &= \mathbb{E} \left\{ \frac{1}{\sqrt{N_r}} \sum_{n_r=1}^{N_r} \mathbf{E}(\mathbf{r}_{n_r}) e^{\frac{j2\pi l(n_r-1)}{N_r}} + \mathbf{n} \right. \\ &\quad \left. \left(\frac{1}{\sqrt{N_r}} \sum_{n'_r=1}^{N_r} \mathbf{E}(\mathbf{r}_{n'_r}) e^{\frac{j2\pi l'(n'_r-1)}{N_r}} + \mathbf{n}' \right)^H \right\} \\ &= \frac{1}{N_r} \sum_{n_r=1}^{N_r} \sum_{n'_r=1}^{N_r} \mathbf{R}_E(\mathbf{r}_{n_r}, \mathbf{r}_{n'_r}) e^{\frac{j2\pi[l(n_r-1)-l'(n'_r-1)]}{N_r}}. \end{aligned} \quad (13)$$

Substitute Eq. (11) into (13), the cross-correlation function between the received signals of different OAM modes can be rewritten as follows:

$$\begin{aligned} \mathbf{R}_y(l, l') &= \frac{1}{N_r} \sum_{n_r=1}^{N_r} \sum_{n'_r=1}^{N_r} e^{\frac{j2\pi[l(n_r-1)-l'(n'_r-1)]}{N_r}} \\ &\quad \sum_{n_t=1}^{N_t} \int_{y_{n_t}-\frac{L}{2}}^{y_{n_t}+\frac{L}{2}} \int_{y_{n_t}-\frac{L}{2}}^{y_{n_t}+\frac{L}{2}} \begin{bmatrix} G^{xy}(\mathbf{r}_{n_r}, \mathbf{s}) \\ G^{yy}(\mathbf{r}_{n_r}, \mathbf{s}) \\ G^{zy}(\mathbf{r}_{n_r}, \mathbf{s}) \end{bmatrix} \begin{bmatrix} G^{xy}(\mathbf{r}_{n'_r}, \mathbf{s}') \\ G^{yy}(\mathbf{r}_{n'_r}, \mathbf{s}') \\ G^{zy}(\mathbf{r}_{n'_r}, \mathbf{s}') \end{bmatrix} ds^y ds'^y. \end{aligned} \quad (14)$$

Eq. (11) can also be rewritten to a discrete form by substituting Eq. (12) into (13) as follows:

$$\begin{aligned} \mathbf{R}_y(l, l') &= \frac{1}{N_r N_l^2} \sum_{n_r=1}^{N_r} \sum_{n'_r=1}^{N_r} e^{\frac{j2\pi[l(n_r-1)-l'(n'_r-1)]}{N_r}} \\ &\quad \sum_{n_t=1}^{N_t} \sum_{n_l=1}^{N_l} \sum_{n'_l=1}^{N_l} \begin{bmatrix} G^{xy}(\mathbf{r}_{n_r}, \mathbf{s}_{n_t, n_l}) \\ G^{yy}(\mathbf{r}_{n_r}, \mathbf{s}_{n_t, n_l}) \\ G^{zy}(\mathbf{r}_{n_r}, \mathbf{s}_{n_t, n_l}) \end{bmatrix} \begin{bmatrix} G^{xy}(\mathbf{r}_{n'_r}, \mathbf{s}_{n_t, n'_l}) \\ G^{yy}(\mathbf{r}_{n'_r}, \mathbf{s}_{n_t, n'_l}) \\ G^{zy}(\mathbf{r}_{n'_r}, \mathbf{s}_{n_t, n'_l}) \end{bmatrix}^H. \end{aligned} \quad (15)$$

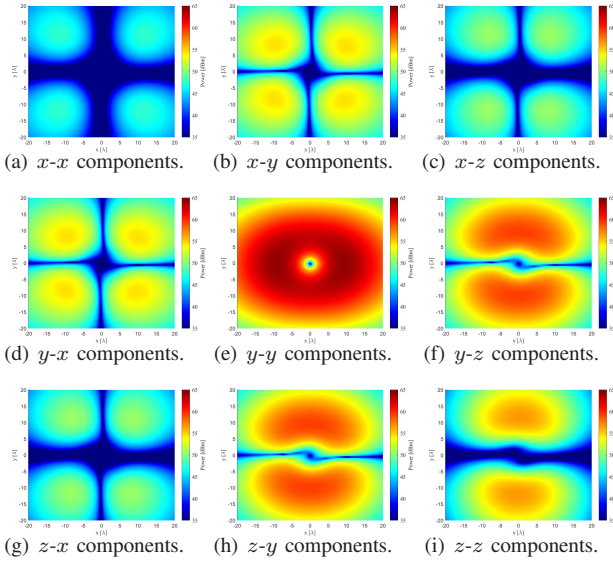


Fig. 5. Powers for autocorrelation functions of OAM-mode 1.

We also plot the power of the autocorrelation functions for OAM mode 1 in Fig. 5, using the same settings as in Fig. 2 based on Eq. (15). As shown, the power for the autocorrelation of the y - y components is significantly higher than that for the autocorrelations of other component combinations.

B. Channel Capacity Derivation

Since the current densities of the sources are aligned along the y -axis, the autocorrelation in the y direction is significantly greater than in any other direction. Thus, in the following sections, we use the cross-correlation between the received signals of different OAM modes and the autocorrelation of the same OAM mode along the y -axis to derive the mutual information and channel capacity. We denote by $R_y(l, l')$ the y component cross-correlation function between the received signals of the l th and l' th OAM modes. $R_y(l, l')$ can be given as follows:

$$\begin{aligned} R_y(l, l') &= \frac{1}{N_r} \sum_{n_r=1}^{N_r} \sum_{n'_r=1}^{N_r} \sum_{n_t=1}^{N_t} e^{\frac{j2\pi[l(n_r-1)-l'(n'_r-1)]}{N_r}} \\ &\quad \sum_{n_t=1}^{N_t} \int_{y_{n_t}-\frac{L}{2}}^{y_{n_t}+\frac{L}{2}} \int_{y_{n_t}-\frac{L}{2}}^{y_{n_t}+\frac{L}{2}} G^{yy}(\mathbf{r}_{n_r}, \mathbf{s}) [G^{yy}(\mathbf{r}_{n'_r}, \mathbf{s}')]^* ds^y ds'^y. \end{aligned} \quad (16)$$

And the discrete form is given as follows:

$$\begin{aligned} R_y(l, l') &= \frac{1}{N_r N_l^2} \sum_{n_r=1}^{N_r} \sum_{n'_r=1}^{N_r} \sum_{n_t=1}^{N_t} e^{\frac{j2\pi[l(n_r-1)-l'(n'_r-1)]}{N_r}} \\ &\quad \sum_{n_t=1}^{N_t} \sum_{n_l=1}^{N_l} \sum_{n'_l=1}^{N_l} G^{yy}(\mathbf{r}_{n_r}, \mathbf{s}_{n_t, n_l}) [G^{yy}(\mathbf{r}_{n'_r}, \mathbf{s}_{n_t, n'_l})]^*. \end{aligned} \quad (17)$$

Therefore, the OAM channel correlation matrix, denoted by \mathbf{R}_{OAM} , can be given as follows:

$$\mathbf{R}_{\text{OAM}} = \begin{bmatrix} R_y(0, 0) & \cdots & R_y(0, N_r - 1) \\ \vdots & \ddots & \vdots \\ R_y(N_r - 1, 0) & \cdots & R_y(N_r - 1, N_r - 1) \end{bmatrix}. \quad (18)$$

Thus, when the transmitted power is evenly distributed to each mode, the channel capacity of the OAM wireless communication with additive white gaussian noise (AWGN), denoted by C , can be given as follows:

$$C = \log_2 \left| \mathbf{I}_{N_r} + \frac{P/N_t}{N_0} \mathbf{R}_{\text{OAM}} \right|, \quad (19)$$

where P denotes the transmitted power and N_0 represents the power of the AWGN.

V. NUMERICAL RESULTS

In this section, we give numerical results to validate the channel capacity enhancement via exploration under EIT framework. We also analyze the impact of various parameters on system performance, including including numbers of transmitting and receiving mode, transmit and receive UCA distance, and UCA radii.

Figure 6 in the next page illustrates the channel capacities of OAM-based wireless communications calculated from both EIT and CIT perspectives, based on the system model presented in Section II. Additionally, we plot the channel capacity of OAM system with transmit and receive UCAs composed of point sources for comparison. The number of transmitting and

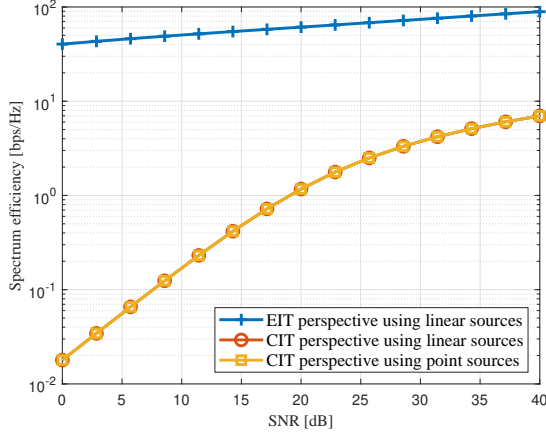


Fig. 6. Enhancement of channel capacity for OAM-based wireless communication from an EIT perspective.

receiving modes is set to 8, and the operating frequency is 5.8 GHz, with a fixed distance of 200λ (10344.8 mm) between the transmit and receive UCAs. Both UCAs are equipped with 8 sources, where each linear source in the transmit UCA consists of 10 small feeds. The current density of each feed in the transmit linear source is normalized by dividing it by $\sqrt{80}$, and the length of each linear source is 0.5λ (25.9 mm). For the point sources, each consists of one small feed, and the current density is normalized by dividing it by $\sqrt{8}$. The radii of both the transmit and receive UCAs are set to $2\lambda/\pi$ (32.9 mm). As depicted in Fig. 6, the EIT method outperforms CIT methods (both with linear and point sources) in terms of spectrum efficiency, particularly at lower SNR values. Among the CIT methods, using linear sources or point sources does not change the channel capacity.

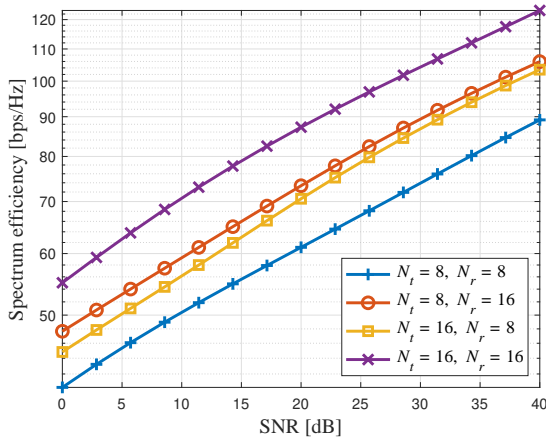


Fig. 7. OAM channel capacities with different numbers of transmitting and receiving mode.

Figure 7 illustrates the channel capacities of the OAM-based wireless communication system, where the number of transmitting and receiving modes alternates between 8 and 16. The operating frequency is also set at 5.8 GHz, and the distance between the transmit and receive UCAs is also fixed

at 200λ (10344.8 mm). The transmit and receive UCAs are equipped with either 8 or 16 antennas. The transmit UCA consists of 10 small feeds. The current density for each feed of the transmit UCA is normalized by dividing it by $\sqrt{10N_t}$. The length of each transmit source is set to 0.5λ (25.9 mm), while the radii of the transmit and receive UCAs are given by $N_t\lambda/(4\pi)$ and $N_r\lambda/(4\pi)$, respectively. Figure 7 compares the spectrum efficiency under four different configurations: $(N_t = 8, N_r = 8)$, $(N_t = 8, N_r = 16)$, $(N_t = 16, N_r = 8)$, and $(N_t = 16, N_r = 16)$. The system's spectrum efficiency increases with SNR across all configurations. As shown in Fig. 7, the configuration with $N_t = 16$ and $N_r = 16$ achieves the highest spectrum efficiency, surpassing 120 bps/Hz at SNR= 40 dB. The performances of the $(N_t = 8, N_r = 16)$ and $(N_t = 16, N_r = 8)$ configurations are nearly identical, though both are lower than that of $(N_t = 16, N_r = 16)$, indicating that increasing neither transmitting and receiving OAM modes can enhance capacity. Notably, increasing the number of receiving OAM modes offers a greater improvement in capacity compared to increasing the number of transmitting OAM modes. The $(N_t = 8, N_r = 8)$ configuration shows the lowest spectrum efficiency, attributed to the fewer OAM modes used for both transmission and reception.

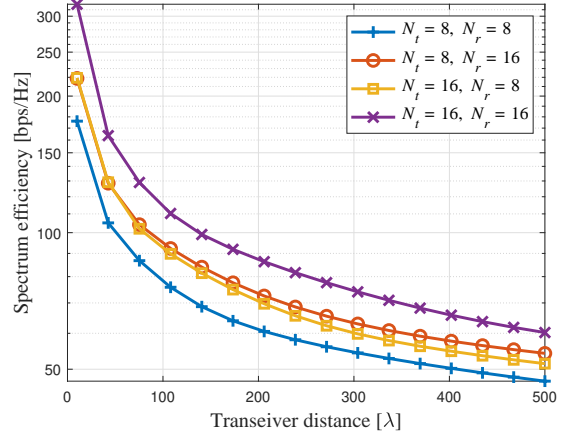
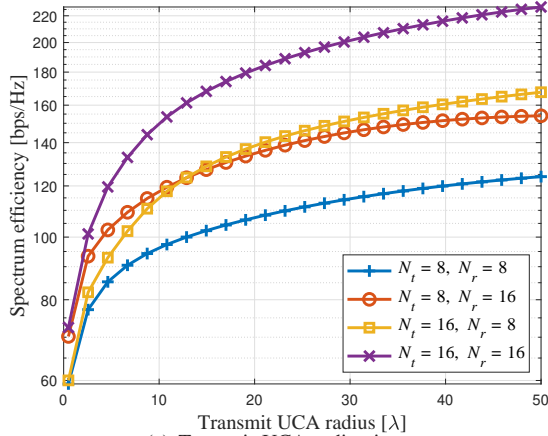
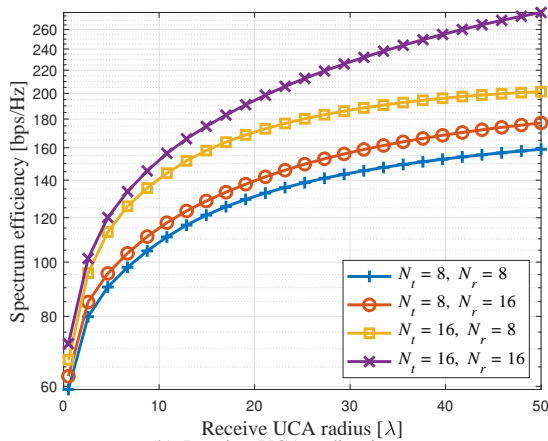


Fig. 8. OAM channel capacities with different transmit and receive UCA distances.

Figure 8 illustrates the OAM channel capacities with the transmit and receive UCA distance varying from 10 to 500λ (517.2 to 25862 mm) for four different configurations of transmitting and receiving modes: $(N_t = 8, N_r = 8)$, $(N_t = 8, N_r = 16)$, $(N_t = 16, N_r = 8)$, and $(N_t = 16, N_r = 16)$. We set SNR = 20 dB. All other parameters remain the same as in Fig. 7. As shown in Fig. 8, all configurations experience a reduction in spectrum efficiency as the transceiver distance increases, which is expected due to propagation losses over longer distances. Among the configurations, $(N_t = 16, N_r = 16)$ consistently achieves the highest spectrum efficiency across all distances. Conversely, the $(N_t = 8, N_r = 8)$ configuration has the lowest spectrum efficiency. The performances of the $(N_t = 8, N_r = 16)$ and $(N_t = 16, N_r = 8)$ configurations remain very similar and closely match that of $(N_t = 16, N_r = 16)$.



(a) Transmit UCA radius impact.



(b) Receive UCA radius impact.

Fig. 9. OAM channel capacities with different transmit and receive UCA radii.

Figure 9 illustrates the impact of different transmit and receive UCA radii on the channel capacity of the OAM-based wireless communication system. The results are also shown for four configurations: $(N_t = 8, N_r = 8)$, $(N_t = 8, N_r = 16)$, $(N_t = 16, N_r = 8)$, and $(N_t = 16, N_r = 16)$. Subplots 9(a) and 9(b) depict the effect of varying the transmit UCA radius and the receive UCA radius from 1 to 50λ (51.7 to 2586.2 mm), respectively, on the system's spectral efficiency. The SNR is set to 20 dB. All other parameters remain the same as in Fig. 7. As shown in Fig. 9(a), all configurations exhibit an increase in spectrum efficiency as the transmit UCA radius increases. Among the configurations, $(N_t = 16, N_r = 16)$ consistently achieves the highest spectrum efficiency across all transmit UCA radii. In contrast, the $(N_t = 8, N_r = 8)$ configuration demonstrates the lowest spectrum efficiency. The performances of $(N_t = 8, N_r = 16)$ and $(N_t = 16, N_r = 8)$ are comparable, although both remain lower than $(N_t = 16, N_r = 16)$ as the UCA radius increases. Notably, $(N_t = 16, N_r = 8)$ exhibits lower spectrum efficiency than $(N_t = 8, N_r = 16)$ when the radius is below 15λ , but surpasses it at larger radii.

Figure 9(b) shows that all configurations exhibit a similar trend of increasing spectrum efficiency as the receive UCA

radius increases. The $(N_t = 16, N_r = 16)$ configuration achieves the highest spectrum efficiency, followed by $(N_t = 16, N_r = 8)$. While the $(N_t = 8, N_r = 16)$ configuration has a lower spectrum efficiency than $(N_t = 16, N_r = 8)$, it grows more rapidly as the receive UCA radius increases. The $(N_t = 8, N_r = 8)$ configuration remains the least efficient across all UCA radii.

VI. SIMULATIONS

In this section, we provide simulations in ANSYS high frequency structure simulator (HFSS). We first give our proposed OAM-NFC simulation model in HFSS. Then, we simulate the electric fields, complex magnitudes, and phase to validate the derivations of electric field in Section. III.

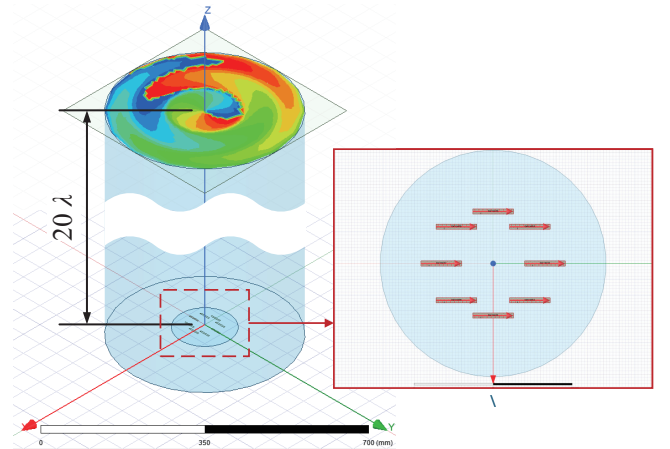


Fig. 10. UCA model and excitations in HFSS.

Figure 10 illustrates the UCA model and excitations simulated in HFSS, where the system operates at a frequency of 5.8 GHz. The distance between the transmit UCA and the observer plane is fixed at 20λ . The radius of the transmit UCA is set to $2\lambda/\pi$, which equals to approximately 32.9 mm. The UCA is configured with 8 linear sources, all aligned along the y -axis. Each linear source has a length of $\lambda/2$ (25.9 mm) and a width of $\lambda/16$ (3.2 mm). The currents are also aligned along the y -axis and are normalized by set the magnitudes as $1/\sqrt{8}$ A.

Figure 11 in the next page illustrates the complex magnitudes of OAM modes -1 , 0 , 1 , and 2 simulated by HFSS. The width of the observer plane is set to 430 mm. All four subplots represent the field distributions in a circular symmetry, with colors changing from red (representing areas of higher field magnitude) to blue (indicating lower magnitudes). The general pattern reveals concentric rings in each plot, highlighting the hollow divergence of OAM beams. The most evident difference lies in the central region. For OAM-mode 0, the field intensity peaks at the center, forming a Gaussian-like distribution, while the other non-zero modes exhibit a central null. OAM modes -1 and 1 are quite similar, each showing a high-power ring around the central null, though the phase and intensity distribution are subtly different due to their opposite OAM modes. OAM-mode 2 displays a more divergent structure, reflecting its higher OAM order.

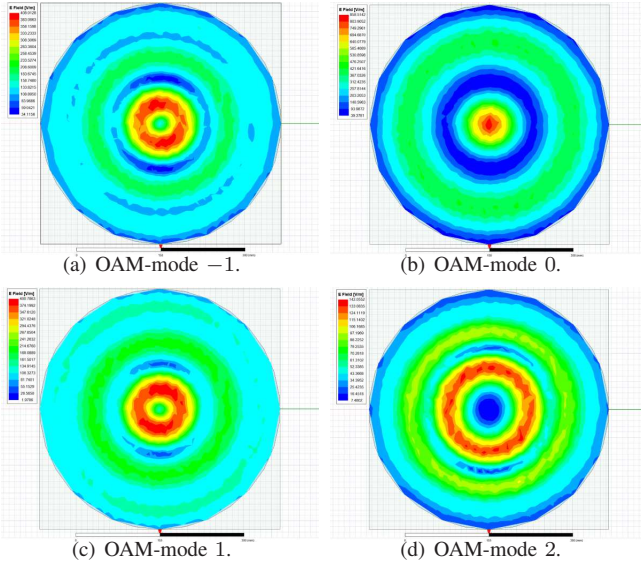


Fig. 11. Complex magnitudes of OAM-mode -1 , 0 , 1 , and 2 simulated by HFSS.

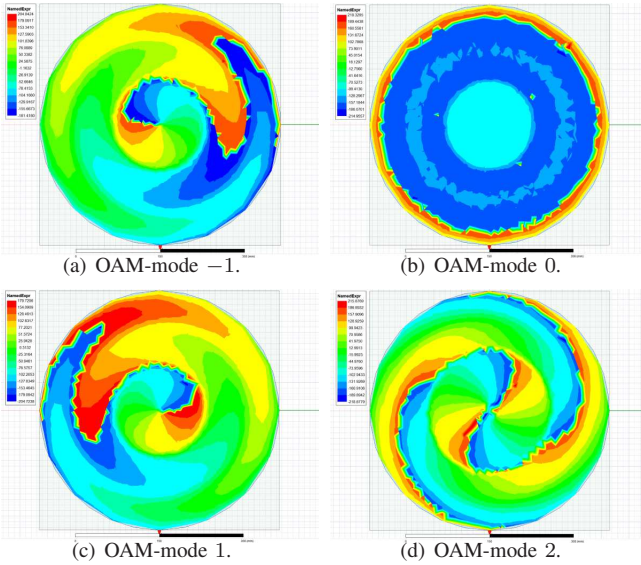


Fig. 12. Phases of y -component electric field for OAM-mode -1 , 0 , 1 , and 2 simulated by HFSS.

Figure 12 depicts the phases of the y -component electric field for OAM modes -1 , 0 , 1 , and 2 , as simulated by HFSS. The width of the observer plane is also set to 430 mm. Across all modes, the color gradient represents the phase variation, with the cyclic transition from red to blue denoting different phase values from -180 to 180 degrees. For OAM-mode 0 , the phase distribution appears uniform. The red central region represents a consistent phase across the field, with minor phase changes toward the edges. In contrast, the non-zero OAM modes -1 , 1 , and 2 exhibit clear spiral phase patterns, a characteristic of OAM-carrying beams. In OAM-mode -1 and OAM-mode 1 , the phase changes smoothly along a helical pattern around the center from -180 to 180 degrees, with -1 and 1 showing opposite rotational directions due to their opposite OAM modes. The spiral pattern becomes

more complex in OAM-mode 2 , with two visible phase twists of 720 degrees, indicating a higher number of phase rotations within the same area. While the OAM mode 0 shows a constant phase distribution, the higher modes reveal distinctive spiral phase variations, with the complexity increasing as the OAM order rises.

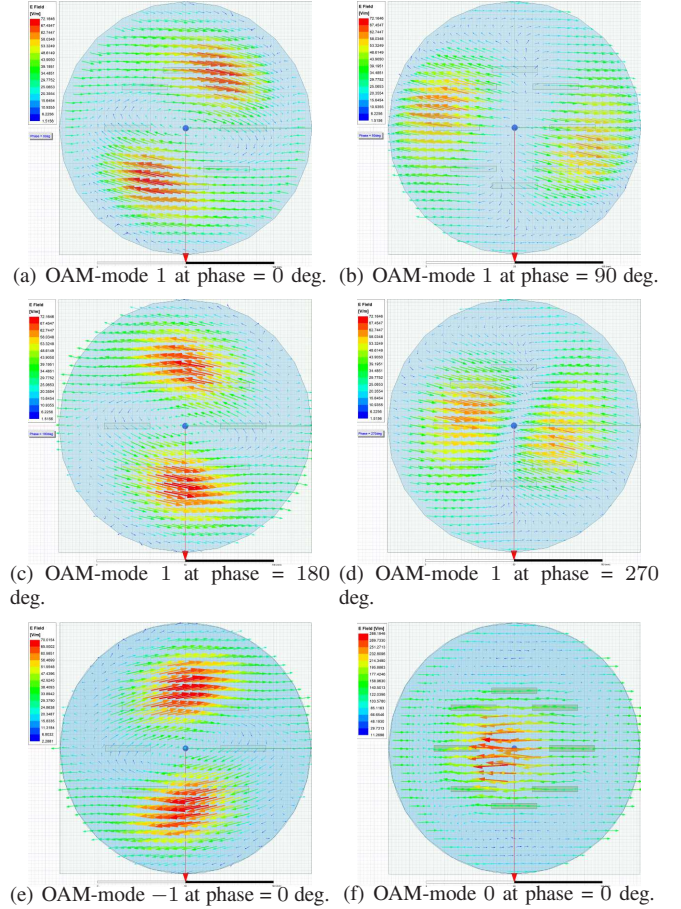


Fig. 13. OAM electric fields at different phases simulated by HFSS.

Figure 13 displays the OAM electric fields at different phases as simulated in HFSS. The width of the observer plane is changed to 144 mm to better show the distribution of the electric field in the center. Figs. 13(a) to 13(d) illustrate the electric fields of OAM-mode 1 at different phases, while Figs. 13(e) and 13(f) show the electric fields of OAM-mode -1 and 0 , respectively, at a phase of 0 degrees. For all subplots, the electric fields are primarily oriented along the y -axis, consistent with the alignment of the current densities in Fig. 3. For OAM-mode 1 in Figs. 13(a) to 13(d), the electric field vectors show significant phase-dependent variations. At phase $= 0$, the electric field distribution is concentrated in two regions near the center, with the vectors pointing outward. As the phase progresses through 90 , 180 , and 270 degrees, these concentrated regions rotate around the center, reflecting the helical structure characteristic of OAM modes. The alternating distribution of the high-intensity red regions indicates the phase-dependent rotation of the electromagnetic field. In Figs. 13(e), OAM-mode -1 at phase $= 0$ exhibits a similar

pattern to OAM-mode 1, but with an opposite rotational direction. This difference underscores the negative OAM sign of this mode. In Figs. 13(f), the electric field of OAM-mode 0 shows a more uniform distribution across the circular plane, with less pronounced vector rotation or localized regions of intensity. This aligns with the nature of OAM mode 0, which lacks OAM, resulting in a more symmetric field structure.

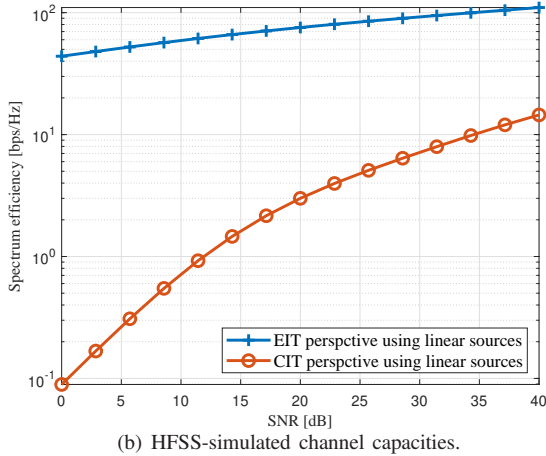
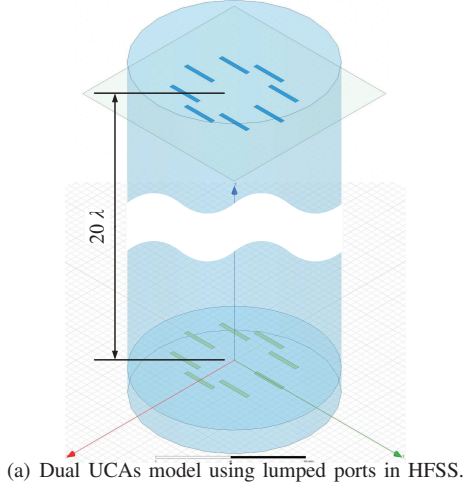


Fig. 14. Enhancement of EIT analyzed channel capacity validated by HFSS simulation.

To validate the enhancement of analyzing OAM channel capacity through EIT in HFSS simulation, we first present a dual UCA model using lumped ports in Fig. 14(a) to calculate the channel capacity from the CIT approach for comparison. As shown in Fig. 14(a), the receive UCA is configured with the same parameters as the transmit UCA shown in Fig. 10. The distance between the transmit and receive UCAs is set to 20λ . All other parameters remain consistent with those in Fig. 10. The S-parameter matrix for the lumped ports, representing the ratios of power waves between the ports, is derived as follows:

$$\mathbf{S} = \begin{bmatrix} S_{1,1} & S_{1,j} & \cdots & S_{1,N_r+N_t} \\ S_{2,1} & S_{2,j} & \cdots & S_{2,N_r+N_t} \\ \vdots & \vdots & \ddots & \vdots \\ S_{i,1} & S_{i,j} & \cdots & S_{i,N_r+N_t} \\ \vdots & \vdots & \ddots & \vdots \\ S_{N_r+N_t,1} & S_{N_r+N_t,j} & \cdots & S_{N_r+N_t,N_r+N_t} \end{bmatrix}, \quad (20)$$

where $S_{i,j} = P_j/P_i$ with P_i and P_j ($1 \leq i, j \leq N_r+N_t$) represent the powers across ports. It is important to note that \mathbf{S} gives the relationships among all ports, including those between each two transmit ports and the return loss. Thus, the channel matrix, denoted by $\mathbf{H}_{\text{lumped}}$, is derived as the square root of the bottom-left quarter of \mathbf{S} , and is given as follows:

$$\mathbf{H}_{\text{lumped}} = \begin{bmatrix} \sqrt{S_{N_t+1,1}} & \sqrt{S_{N_t+1,2}} & \cdots & \sqrt{S_{N_t+1,N_t}} \\ \sqrt{S_{N_t+2,1}} & \sqrt{S_{N_t+2,2}} & \cdots & \sqrt{S_{N_t+2,N_t}} \\ \vdots & \vdots & \ddots & \vdots \\ \sqrt{S_{N_t+N_r,1}} & \sqrt{S_{N_t+N_r,2}} & \cdots & \sqrt{S_{N_t+N_r,N_t}} \end{bmatrix}. \quad (21)$$

Therefore, the channel capacity of OAM using linear sources analyzed by CIT, denoted by C_{CIT} , can be given as $C_{\text{CIT}} = \log_2 \left| \mathbf{I}_{N_r} + \frac{P/N_t}{N_0} \mathbf{R}_{\text{lumped}} \right|$, where $\mathbf{R}_{\text{lumped}}$ denotes the correlation matrix and is given as $\mathbf{R}_{\text{lumped}} = \mathbf{W}^H \mathbf{H}_{\text{lumped}} \mathbf{W} \left(\mathbf{W}^H \mathbf{H}_{\text{lumped}} \mathbf{W} \right)^H$.

Figure 14(b) illustrates the HFSS-simulated channel capacities for OAM-based wireless communications, calculated using both EIT and CIT approaches, respectively. The OAM channel capacity analyzed by CIT is derived from the S-parameters of the dual UCA model in Fig. 14(a). The OAM channel capacity analyzed by EIT is calculated based on the export electric fields of the UCA model shown in Fig. 10. Specifically, to compute the channel capacity using EIT, signals are transmitted across 8 OAM modes, ranging from -3 to 4 . Then, HFSS is used to export the electric field at 8 evenly distributed points on a circle with a radius R_r , located 20λ (1034.5 mm) away from the transmit UCA, which corresponds to the receive UCA as defined in Section II. Using the DFT transformation of the electric field, the channel matrix and correlation matrix between each transmitting and receiving mode are obtained. The channel capacity is then calculated following Eq. (19). As shown in Fig. 14(b), the EIT method outperforms the CIT method in terms of spectrum efficiency, particularly at lower SNR values. These results are highly consistent with the numerical findings presented in Fig. 6, demonstrating the huge improvement in capacity of analyzing OAM through EIT compared to CIT.

Figure 15(a) in the next page presents a transmit UCA model in HFSS equipped with 16 linear sources and a radius of $4\lambda/\pi$ (65.86 mm). Based on the models in Figs. 10 and 15(a), we plot Fig. 15(b), illustrating the channel capacities of an OAM-based wireless communication system, where the number of transmitting and receiving modes alternates between 8 and 16, and the SNR is set to 20 dB. All other parameters match those in Fig. 14(b). Consistent with the numerical results in Fig. 7, an increase in either transmitting or receiving modes enhances channel capacity in Fig. 15(b). When both N_t and N_r are set to 16, the system achieves significantly higher spectral efficiency compared to configurations with fewer transmitting or receiving modes. The configuration with $N_t = 8$ and $N_r = 8$ yields the lowest capacity. However, when N_r increases to 16 while keeping $N_t = 8$, capacity improves only slightly. This result differs from Fig. 7 due to the variation in transmitter-receiver distance. Increasing N_t to 16 with $N_r = 8$ significantly boosts capacity, as the higher number of transmitting modes enhances orthogonal

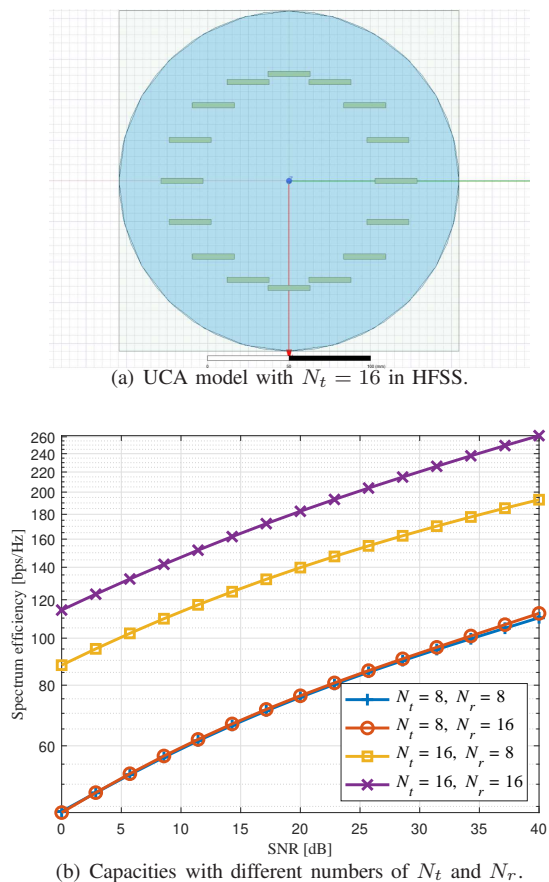


Fig. 15. HFSS-simulated OAM channel capacities with different numbers of transmitting and receiving mode.

channel availability. In summary, both N_t and N_r positively impact system capacity, although an increase in N_t alone notably improves capacity, whereas an increase in N_r alone has minimal impact.

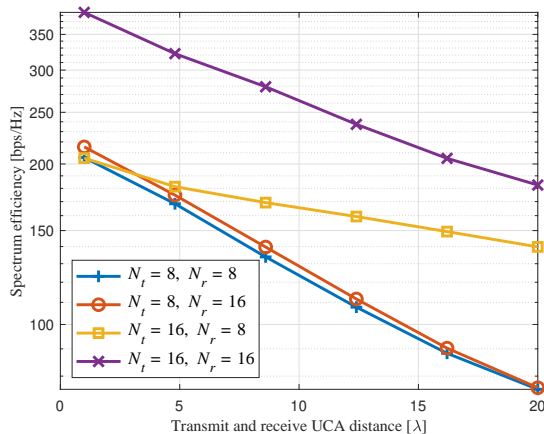


Fig. 16. HFSS-simulated OAM channel capacities with different transmit and receive UCA distances.

Figure 16 depicts the OAM channel capacities for varying distances between the transmit and receive UCAs, ranging from 1λ (51.7 mm) to 20λ (1034.5 mm), across four configurations of transmitting and receiving modes: ($N_t =$

$8, N_r = 8$), ($N_t = 8, N_r = 16$), ($N_t = 16, N_r = 8$), and ($N_t = 16, N_r = 16$). All other parameters remain consistent with those in Fig. 15(b). In Fig. 16, the channel capacities decrease for all configurations as the transmit-receive UCA distance increases, aligning with the numerical results in Fig. 8. The configuration with both $N_t = 16$ and $N_r = 16$ consistently achieves the highest spectral efficiency across all distances. Configurations with $N_t = 8$ exhibit lower spectral efficiencies and experience more pronounced capacity declines as the distance increases, eventually converging at longer distances. The configuration where $N_t = 16$ and $N_r = 8$ shows intermediate performance, with capacities higher than the $N_t = 8$ cases but not as high as when both N_t and N_r are set to 16.

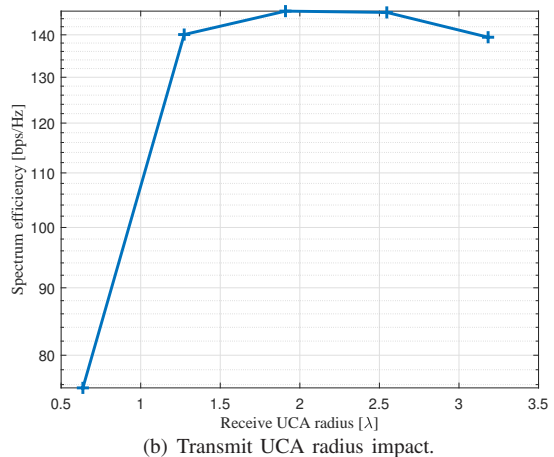
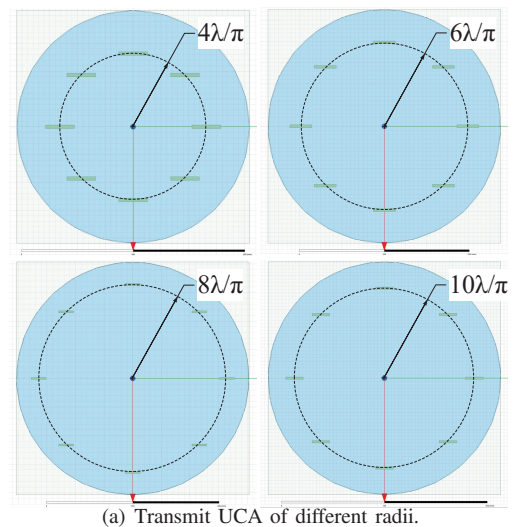


Fig. 17. HFSS-simulated OAM channel capacities with different transmit UCA radii.

To analyze the impact of the transmit UCA radius on OAM channel capacities, we model four UCAs with different transmit UCA radii, ranging from $4\lambda/\pi$ (65.9 mm) to $10\lambda/\pi$ (164.6 mm), as shown in Fig. 17(a). Based on results from the models in Figs. 10 and 17(a), Fig. 17(b) illustrates the effect of varying transmit UCA radii on the channel capacity of the OAM-based wireless communication system. As depicted in Fig. 17(b), an increase in the transmit UCA radius leads to

a noticeable improvement in channel capacity, with a sharp rise in spectrum efficiency as the radius grows from $2\lambda/\pi$ (32.9 mm) to $4\lambda/\pi$ (65.9 mm), consistent with the numerical results. However, after peaking between $6\lambda/\pi$ (98.8 mm) and $8\lambda/\pi$ (131.7 mm), further increases in radius result in a slight decrease or leveling off in spectrum efficiency.

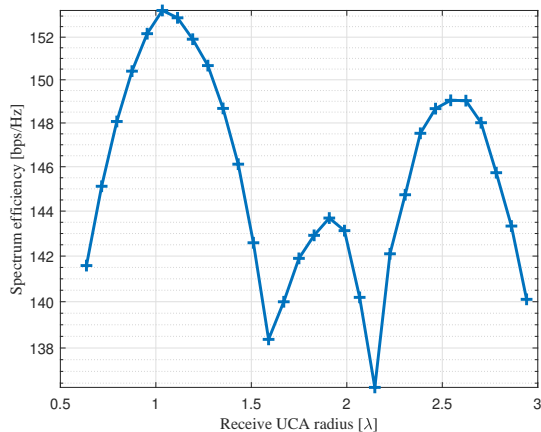


Fig. 18. HFSS-simulated OAM channel capacities with different receive UCA radii.

Figure 18 illustrates how the OAM channel capacity varies with receive UCA radius. Unlike the numerical results shown in Fig. 9(b), Fig. 18 reveals a non-monotonic relationship between receive UCA radius and spectrum efficiency, with multiple peaks and valleys. This fluctuation suggests that certain receive UCA radii enhance channel capacity while others may reduce performance. The variation occurs because each OAM mode has a unique maximum power radius and several sub-high power radii. These results highlight the sensitivity of the OAM channel to changes in receive UCA radius and underscore the importance of optimizing the receive UCA radius to maximize system performance.

VII. CONCLUSIONS

In this paper, we analyzed OAM-based wireless communications from an EIT perspective because of its advantages of integrating electromagnetic theory and CIT. The induced electric field of OAM signal was derived by using Green's function. We then derived the channel capacity for OAM-based wireless communication by presenting the autocorrelation and cross-correlation functions of the received OAM signals. Numerical and simulation results validated the channel capacity enhancement via exploration under EIT framework. Furthermore, we analyzed the impact of various parameters on the channel capacity, including numbers of transmitting and receiving mode, transmit and receive UCA distance, and UCA radius. These findings provide valuable insights into the performance and capacity benefits of OAM-based systems analyzed through EIT.

REFERENCES

[1] L. Allen, M. Beijersbergen, R. Spreeuw, and J. P. Woerdman, "Orbital angular momentum of light and transformation of Laguerre Gaussian laser modes," *Physical review A*, vol. 45, pp. 8185–8189, July 1992.

[2] B. Thide, H. Then, J. Sjöholm, K. Palmer, J. Bergman, T. D. Carozzi, Y. Istomin, N. Ibragimov, and R. Khamitova, "Utilization of photon orbital angular momentum in the low-frequency radio domain," *Physical review letters*, vol. 99, pp. 087 701–087 701, Aug. 2007.

[3] K. A. Opare, Y. Kuang, and J. J. Kponyo, "Mode combination in an ideal wireless OAM-MIMO multiplexing system," *IEEE Wireless Communications Letters*, vol. 4, no. 4, pp. 449–452, Aug. 2015.

[4] R. Lyu, W. Cheng, and W. Zhang, "Modeling and performance analysis of OAM-NFC systems," *IEEE Transactions on Communications*, vol. 69, no. 12, pp. 7986–8001, 2021.

[5] R. Lyu, W. Cheng, M. Wang, and W. Zhang, "Fractal OAM generation and detection schemes," *IEEE Journal on Selected Areas in Communications*, vol. 42, no. 6, pp. 1598–1612, 2024.

[6] R. Lyu, W. Cheng, B. Shen, Z. Ren, and H. Zhang, "OAM-SWIPT for IoE-Driven 6G," *IEEE Communications Magazine*, vol. 60, no. 3, pp. 19–25, 2022.

[7] C. E. Shannon, "A mathematical theory of communication," *The Bell System Technical Journal*, vol. 27, no. 3, pp. 379 – 423, July 1948.

[8] J. Zhu, Z. Wan, L. Dai, M. Debbah, and H. V. Poor, "Electromagnetic information theory: Fundamentals, modeling, applications, and open problems," *IEEE Wireless Communications*, vol. 31, no. 3, pp. 156–162, 2024.

[9] W. Cheng, W. Zhang, H. Jing, S. Gao, and H. Zhang, "Orbital angular momentum for wireless communications," *IEEE Wireless Communications Magazine*, vol. 26, no. 1, pp. 100–107, Feb. 2019.

[10] H. Jing, W. Cheng, X.-G. Xia, and H. Zhang, "Orbital-angular-momentum versus MIMO: Orthogonality, degree of freedom, and capacity," in *2018 IEEE 29th Annual International Symposium on Personal, Indoor and Mobile Radio Communications (PIMRC)*, 2018, pp. 1–7.

[11] O. Edfors and A. J. Johansson, "Is orbital angular momentum (OAM) based radio communication an unexploited area?" *IEEE Transactions on Antennas and Propagation*, vol. 60, no. 2, pp. 1126–1131, 2012.

[12] A. Poon, R. Brodersen, and D. Tse, "Degrees of freedom in multiple-antenna channels: a signal space approach," *IEEE Transactions on Information Theory*, vol. 51, no. 2, pp. 523–536, 2005.

[13] F. K. Gruber and E. A. Marengo, "New aspects of electromagnetic information theory for wireless and antenna systems," *IEEE Transactions on Antennas and Propagation*, vol. 56, no. 11, pp. 3470–3484, 2008.

[14] Z. Zhang, Y. Xiao, Z. Ma, M. Xiao, Z. Ding, X. Lei, G. K. Karagiannidis, and P. Fan, "6G wireless networks: Vision, requirements, architecture, and key technologies," *IEEE Vehicular Technology Magazine*, vol. 14, no. 3, pp. 28–41, 2019.

[15] Z. Yao, W. Cheng, W. Zhang, and H. Zhang, "Resource allocation for 5G-UAV-based emergency wireless communications," *IEEE Journal on Selected Areas in Communications*, vol. 39, no. 11, pp. 3395–3410, 2021.

[16] L. Zhou, S. Leng, Q. Liu, and Q. Wang, "Intelligent UAV swarm cooperation for multiple targets tracking," *IEEE Internet of Things Journal*, vol. 9, no. 1, pp. 743–754, 2022.

[17] C.-X. Wang, Y. Yang, J. Huang, X. Gao, T. J. Cui, and L. Hanzo, "Electromagnetic information theory: Fundamentals and applications for 6g wireless communication systems," *IEEE Wireless Communications*, vol. 31, no. 5, pp. 279–286, 2024.

[18] A. Sayeed and N. Behdad, "Continuous aperture phased MIMO: Basic theory and applications," in *2010 48th Annual Allerton Conference on Communication, Control, and Computing (Allerton)*, 2010, pp. 1196–1203.

[19] Z. Zhang and L. Dai, "Pattern-division multiplexing for continuous-aperture MIMO," in *ICC 2022 - IEEE International Conference on Communications*, 2022, pp. 3287–3292.

[20] S. Hu, F. Rusek, and O. Edfors, "Beyond massive MIMO: The potential of data transmission with large intelligent surfaces," *IEEE Transactions on Signal Processing*, vol. 66, no. 10, pp. 2746–2758, 2018.

[21] C. Huang, A. Zappone, G. C. Alexandropoulos, M. Debbah, and C. Yuen, "Reconfigurable intelligent surfaces for energy efficiency in wireless communication," *IEEE Transactions on Wireless Communications*, vol. 18, no. 8, pp. 4157–4170, 2019.

[22] T. Yuan, Y. Cheng, H. Wang, and Y. Qin, "Mode characteristics of vortical radio wave generated by circular phased array: Theoretical and experimental results," *IEEE Transactions on Antennas and Propagation*, vol. 65, no. 2, pp. 688–695, Feb. 2017.

[23] Z. Wan, J. Zhu, Z. Zhang, L. Dai, and C.-B. Chae, "Mutual information for electromagnetic information theory based on random fields," *IEEE Transactions on Communications*, vol. 71, no. 4, pp. 1982–1996, 2023.